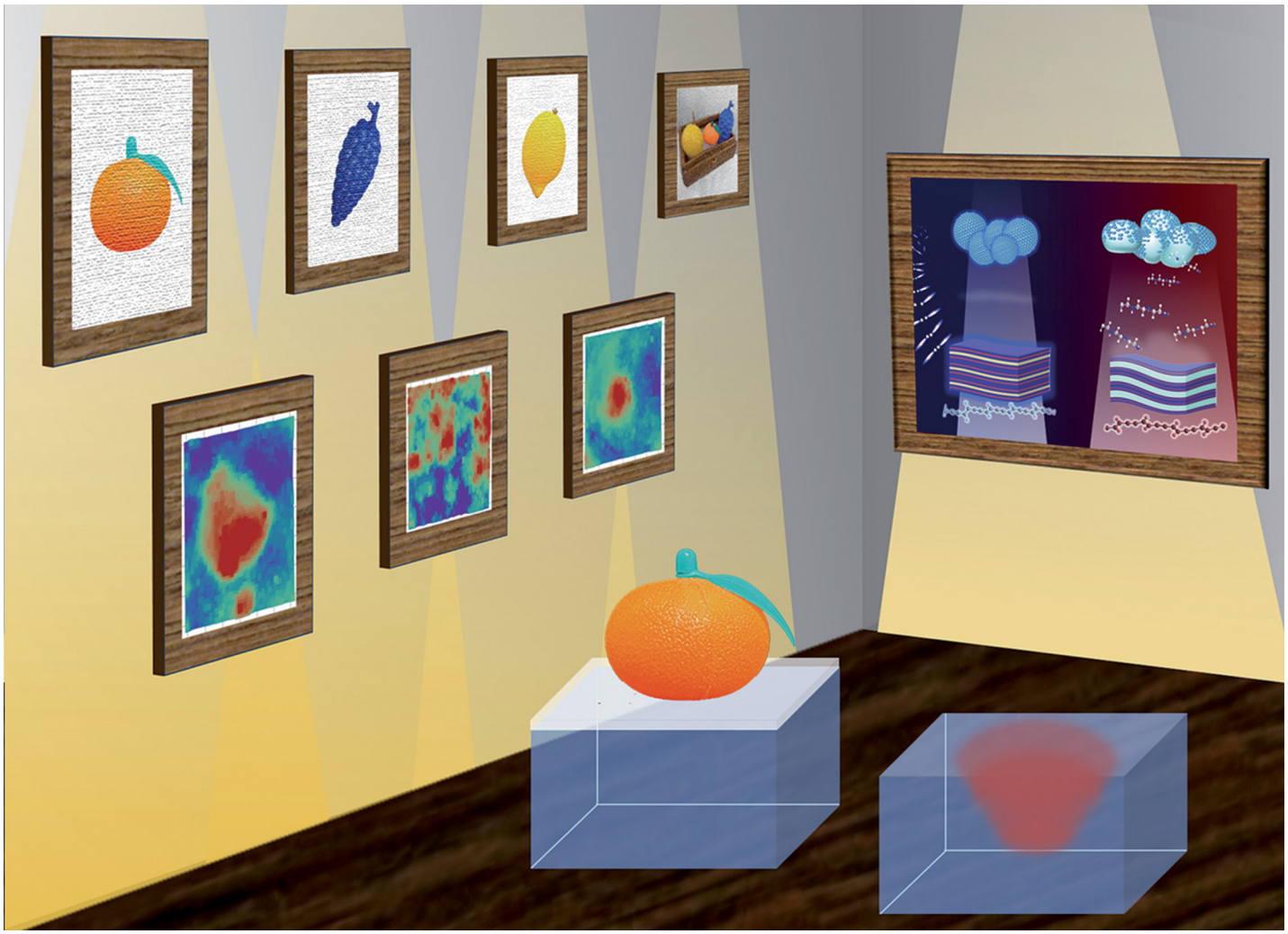

Showcasing research from Professor Yuya Oaki's group at Department of Applied Chemistry, Faculty of Science and Technology, Kaio University, Japan.

2D stress-distribution imaging using 3D transparent stimulus-responsive color-changing rubber

We report 2D distribution imaging of compression stresses applied by 3D irregularly shaped objects. Such imaging is now only found in the world of computer simulation. In the present work, a transparent 3D rubber device combining stimuli-responsive materials enables stress distribution imaging in the real world.

Image reproduced by permission of Yuya Oaki from *Mater. Horiz.*, 2026, **13**, 3326.

As featured in:

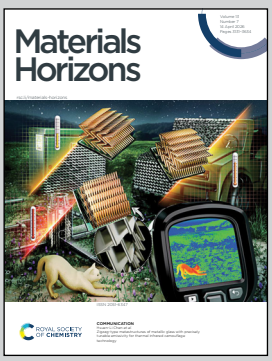

See Syuji Fujii, Yuya Oaki *et al.*, *Mater. Horiz.*, 2026, **13**, 3326.

ROYAL SOCIETY OF CHEMISTRY

rsc.li/materials-horizons

Registered charity number: 207890

Materials Horizons

ROYAL SOCIETY OF CHEMISTRY

COMMUNICATION

View Article Online
View Journal | View Issue

Cite this: *Mater. Horiz.*, 2026, **13**, 3326

Received 27th November 2025,
Accepted 24th February 2026

DOI: 10.1039/d5mh02253c

rsc.li/materials-horizons

2D stress-distribution imaging using 3D transparent stimulus-responsive color-changing rubber

Hazuki Yamanaka,[a] Hiroaki Imai,[a] Syuji Fujii *[bc] and Yuya Oaki *[a]

Imaging of invisible mechanical stresses is a significant challenge in a variety of fields. 2D distribution imaging of compression stresses applied by irregularly shaped 3D objects is not achieved using conventional sensing materials and devices. In the present work, such a compression-stress distribution in the range of 0.1 kPa–5 MPa is imaged using 3D transparent silicone rubber containing stimuli-responsive color-changing conjugated polymer, layered polydiacetylene (PDA). Compression-responsive capsules, liquid droplets surrounded by solid particles, collapse with compression on the rubber. The outflowed interior liquid containing polyethyleneimine (PEI) oligomer is diffused into the bulk rubber through the free volume space of the rubber matrix. PEI serves as a guest for intercalation into the interlayer space of the layered PDA, *i.e.* chemical stress, directing the blue-to-red color change. As the red-color intensity increases with increasing applied compression stress, the strength is colorimetrically quantified. The transparent 3D device enables 2D distribution imaging of the compression stresses applied by irregularly shaped 3D objects in the millimeter to the centimeter scales. The device design can be applied to achieve 2D stress-distribution imaging in various length scales and strength ranges.

New concepts

The present work shows a new concept of force-distribution imaging. A transparent 3D rubber containing stimuli-responsive color-changing material enables 2D distribution imaging and quantification of compression stresses applied by irregularly shaped 3D objects. Such imaging and quantification are only achieved using computer simulation. In previous works, stimuli-responsive color-changing materials and their 2D film devices were prepared to detect compression stresses. However, the distribution imaging of stresses applied by irregularly shaped 3D probes was not achieved because the devices were not strained with sufficient conformity to the 3D shapes of the compressing probes. In the real world, compression stresses are applied using 3D objects with complex shapes. A new concept is required to design stress sensors for imaging and quantifying the force distribution. Visualizing invisible forces has been a significant challenge in the fields of biological, medical, and physical sciences. We propose the use of a stimuli-responsive color-changing 3D device with both sufficient transparency and elasticity for the distribution imaging and quantification of the compression stresses. Force sensors covering the diverse types, ranges, and scales can be realized based on the present design concept.

Introduction

Sensing the spatiotemporal distribution of forces is significant in a broad range of fields, such as science, technology, medicine, arts, and sports.[1–3] Distribution imaging contributes to analyzing the skilfull motion of professionals and degradation of materials.[1–4] However, the development of such imaging devices and technologies still remains challenging because force has diverse applied types, strength ranges, and length scales.[2,5,6] A suitable sensing device is required depending on the targets. For example, appropriate thermometry or thermography is selected depending on the targeted temperature range and imaging area. In contrast to thermal sensing, mechano-sensing devices are not fully prepared to cover diverse types, ranges, and scales. Therefore, the development of new materials, devices, and methodologies is required to advance mechano-sensing (Fig. 1).

In recent years, wearable flexible electronic devices have been extensively studied for monitoring motions.[7–9] These electronic devices detect strain using current or capacitance as an output signal. Although the applied stresses and strains are detected in real time with high sensitivity, the distribution is not imaged by these devices. Digital imaging correlation is used to visualize distribution of strain particularly in large-scale architectures.[10,11] A speckle pattern is coated on the target

[a] *Department of Applied Chemistry, Faculty of Science and Technology, Keio University, 3-14-1 Hiyoshi, Kohoku-ku, Yokohama 223-8522, Japan. E-mail: oakiyuya@applc.keio.ac.jp*

[b] *Department of Applied Chemistry, Faculty of Engineering, Osaka Institute of Technology, 5-16-1 Omiya, Asahi-ku, Osaka 535-8585, Japan. E-mail: syuji.fujii@oit.ac.jp*

[c] *Department of Chemistry, Faculty of Science, Chulalongkorn University, Bangkok 10330, Thailand*

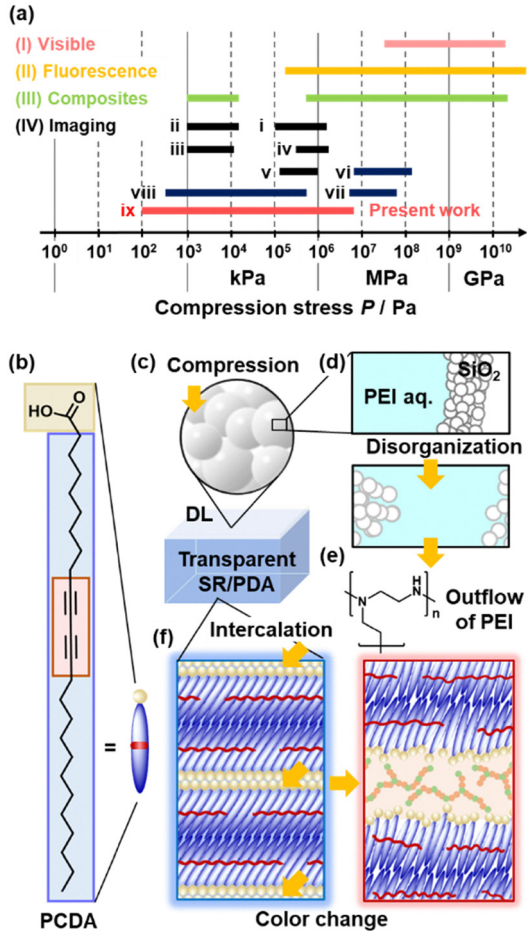

Fig. 1 Summary of mechanoresponsive materials in the earlier works (a) and our materials design in the present work (b)–(f). (a) Four types of compression-responsive materials and their detection ranges (the works (i)–(viii) correspond to the ref. 19–26). (b) PCDA monomer forming the layered structure. (c) SR/PDA device with dispersion of DL on the top face. (d) DL consisting of the silica shell and interior liquid (upper) and its compression-induced disorganization leading to the outflow of the interior liquid (lower). (e) PEI oligomer in the interior liquid. (f) Intercalation of PEI in the interlayer space of PDA leading to the color change.

material, and its change is observed using a camera while applying stresses. The image is not obtained in the area overlapping the coating pattern and compressing probe. Whereas these devices enable the real-time stress sensing, the applied stresses are not recorded in the devices. The present work shows a chemical 3D sensing device for visible 2D distribution imaging of compression stresses in the range of 10^2–10^6 Pa at the millimeter to the centimeter scales (Fig. 1). The irreversible color-changing behavior enables recording of the applied stresses.

Mechanoresponsive molecules and materials have been studied to achieve visible and/or fluorescence detection of mechanical stresses, such as frictional, compressive, and tensile stresses.[12–18] The quantitative and qualitative detections of compression stresses have been demonstrated using a few techniques: visible detection without UV excitation (type I), fluorescence (type II), and polymer composite containing chromophores (type III) (Fig. 1a). The detailed literature information is provided in Fig. S1 in the SI. The detection range of the compression stress is higher than 10^5 Pa for the conventional approaches in the previous works except in one report (Fig. S1 in the SI). In contrast, the distribution imaging, both quantification and visualization, has been studied in a limited number of previous works (type IV in Fig. 1a).[19–26] Although the imaging was performed in the works (i) and (iii) in the type (IV),[19,21] the measured force was not quantified. The distribution imaging was carried out in the works (ii), (iv), and (v).[20,22,23] Our group reported the imaging in the works (vi)–(viii).[24–26] However, these previous works show 2D distribution imaging using the 2D thin devices. 3D objects are not used as compressing probes. The 2D distribution imaging using soft transparent 3D devices was not achieved in previous works. The length scale and strength range are still limited to the diversity of forces. In the present work, a 3D transparent rubber containing PDA has been developed for 2D stress distribution imaging with a wider detection range ((ix) in Fig. 1a).

PDA exhibits blue-to-red color changes in response to stimuli, such as thermal, chemical, and frictional stresses, through shortening the effective conjugation length.[26–34] A variety of diacetylene (DA) monomers and their assembly states have been studied to control the stimuli responsivity.[26–34] Whereas PDA shows direct responsiveness to frictional stress,[35,36] only a specific DA monomer provided PDA with the responsiveness to compression stress.[37] Our group reported that by combining other stimuli-responsive materials the responsiveness to tensile and compression stresses can be exhibited.[38–40] However, 2D imaging of compression stresses applied by irregularly shaped 3D objects has not been achieved. In the present work, a compression-responsive capsule material, dry liquid (DL), was used to demonstrate the distribution imaging by combining with the transparent SR containing PDA (Fig. 1b–f). DL consists of liquid droplets coated by solid particles (Fig. 1c and d). The interior liquid containing PEI is flowed out of the capsule *via* disruption triggered by compression (Fig. 1d and e). The outflowing PEI oligomer is penetrated and diffused into the bulk SR matrix through the free volume space (Fig. 1e and f), PDA dispersed in SR showed color changes with intercalating PEI. Therefore, the DL/SR/PDA transparent 3D rubber device enables 2D distribution imaging of the compression stress. These design strategies of the devices can be applied to develop a variety of stress-distribution imaging sensors.

Results and discussion

Device design for 2D stress-distribution imaging

Here we focus on dimensions of the probe, the device, and distribution imaging for compression stresses (Fig. 2a–d). Stimuli-responsive color-changing 2D films enable detection of the compression stresses applied *via* 2D and 3D probes and colorimetric quantification based on the intensity of color (I) (Fig. 2a and b). However, the distribution imaging of stresses applied by irregularly shaped 3D objects cannot be achieved because the thin film is not fully strained with the conforming

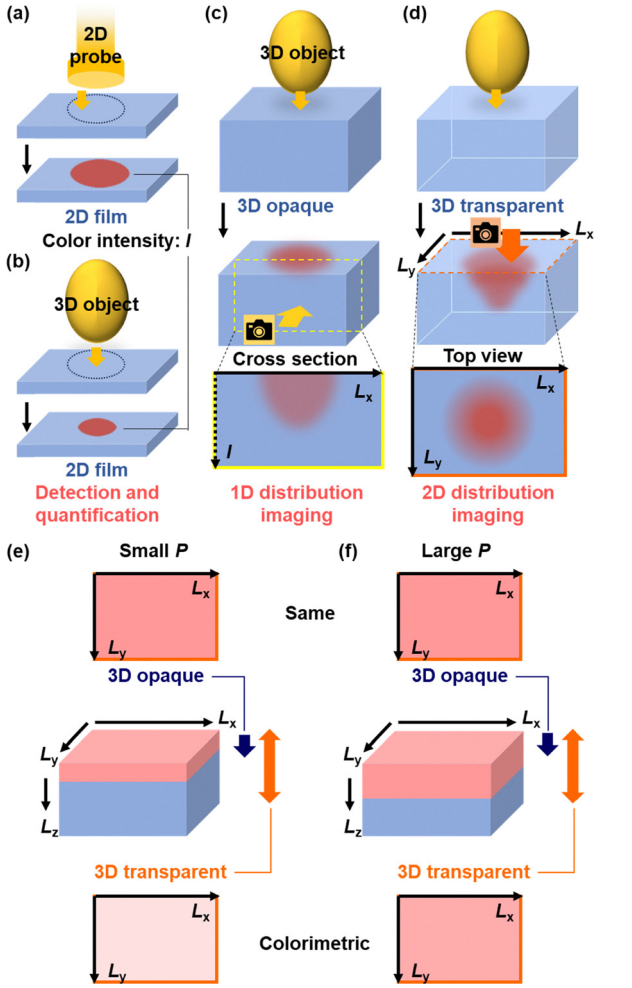

Fig. 2 Device design for distribution imaging of compression stresses. (a) and (b) 2D film devices with compression by a 2D probe (a) and a 3D object (b). (c) 3D opaque device providing the distribution imaging on a certain cross-section with compression by a 3D object. (d) 3D transparent device providing the 2D distribution imaging with compression by a 3D object (the present work). (e) and (f) Comparison of the imaging on the surface using 3D opaque (upper panels) and transparent (lower panels) devices with applying small (e) and large (f) *P*.

shape (Fig. 2b). Therefore, 3D soft devices are required to image the stress distribution applied *via* 3D objects (Fig. 2c and d). In our previous works,[24,27] a 3D sponge was used to visualize stress distribution on a certain cross-section of the device (Fig. 2c). The cross-sectional image represents the relationship between the coordinate (L_x) and I as 1D stress-distribution imaging. However, the 2D distribution is not imaged on the top-face of the sponge device because the interior of the sponge is opaque. In the present work, a transparent 3D silicone rubber (SR) containing layered PDA enables 2D distribution imaging of compression stresses originating from irregularly shaped 3D objects in the L_x–L_y coordinate (Fig. 2d).

The transparency of the device is an important factor in 2D stress-distribution imaging. When different strengths of compression stresses are applied to the 3D device, the color-changes in areas in the depth direction are different in principle (the middle illustrations in Fig. 2e and f). A stronger stress induces the color change in a deeper area of the device (Fig. 2f). If the transparency of the device is insufficient (dark blue arrow in the middle of Fig. 2e and f), the differences in the color-changes in the area in the depth direction are not clearly visualized by the color intensity on the surface image. Only the color change near the surface is detected using the photograph. On the other hand, the transparent device can visualize the differences in the color-changes in the area in the depth direction *via* the color intensity on the surface image (orange arrow in the middle of Fig. 2e and f). Therefore, the colorimetric 2D stress distribution imaging can be achieved using a 3D transparent device.

If the color-change behavior in response to the applied stimuli is reversible and momentary, real-time force monitoring can be achieved. Such a sensing device is applied to analyze motions using professionals and robots. On the other hand, irreversible color-change behavior is used for the cumulative recording of the applied stresses, regardless of the response time. This type of device enables analyzing the strength and distribution of the stresses applied and accumulated in the device colorimetrically. In the present work, as PDA shows irreversible color change, the applied stress can be recorded as a red-color distribution in the SR matrix.

Transparent silicone rubber containing PDA

A silicone rubber containing PDA was prepared using a commercial poly(dimethylsiloxane) (PDMS) precursor and a curing agent *via* an addition reaction.[41] The detailed procedure is described in the SI. A chloroform solution of 10,12-pentacosadiynoic acid (PCDA), which is one of amphiphilic DA monomers, was added to the silicone precursor. After evaporation of chloroform under a vacuum, PCDA was topochemically polymerized using UV irradiation (254 nm, 6 W) under mixing to obtain PDA. The SR matrix transmitted in the UV region at around 250 nm to induce the topochemical polymerization of PCDA (Fig. S2 in the SI). The curing agent was added to the PDMS matrix with dispersion of PDA under stirring. After the mixture was maintained thus for 3 days, SR containing PDA (SR/PDA) was obtained. SR/PDA was cut into pieces of 10 × 10 × 3 mm in size (Fig. 3a). The photographs and optical microscopy images of SR/PDA show a homogenous blue color characteristic of PDA (Fig. 3a and b). The dark-blue PDA crystals were homogenously dispersed in the SR matrix (Fig. 3b and c). The PDA crystals, measuring 20.3 ± 8.9 μm longitudinally, were observed on the back scattered electron (BSE) image using scanning electron microscopy (SEM) (Fig. 3d).

In the SR matrix, PDA formed the layered structure (Fig. 3e). The PCDA monomer in the powdered state showed X-ray diffraction (XRD) peaks at 2θ = 1.89, 5.64, 9.38, and 13.1° characteristic of the layered structure with the interlayer distance d_0 = 4.67 nm (circles in Fig. 3e). A weak peak at 2θ = 1.87°, corresponding to d_0 = 4.72 nm, was observed for SR/PDA, whereas SR had only the broadened halo around 2θ = 12° (Fig. 3e). Raman spectra support the formation of PDA in the SR matrix (Fig. 3f). The PCDA monomer and PDA showed

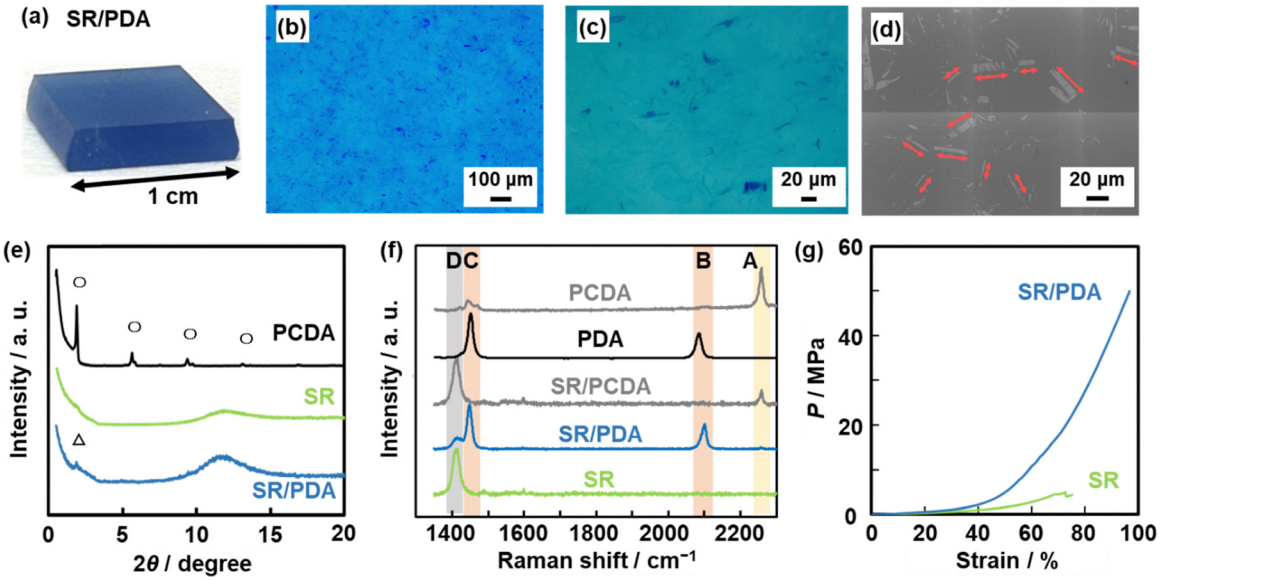

Fig. 3 Structural analysis of SR/PDA. (a) Photograph. (b) and (c) Optical microscopy and its magnified images. (d) Combined BSE (SEM) image with tiling the original images. (e) XRD patterns of the reference PCDA powder (black), SR (green), and SR/PDA (blue). (f) Raman spectra of the reference PCDA powder (gray), PDA powder (black), SR/PCDA (gray), SR/PDA (blue), and SR (green). (g) Stress–strain curves of SR/PDA (blue) and SR (green) with compression.

Raman peaks at 2260 cm^{-1} assignable to the C≡C stretching vibration (band A in Fig. 3f) and at 1450 and 2080 cm^{-1} assignable to the ene–yne structure (bands B and C in Fig. 3f), respectively. PDA in the SR matrix showed the peaks at 1450 and 2080 cm^{-1} (bands B and C) in addition to that at 1410 cm^{-1} assignable to the C–H asymmetric bending vibration of PDMS (band D in Fig. 3f).[42]

The stress–strain curve of SR/PDA with compression indicates that the mechanical strength of SR was improved by inclusion of PDA (Fig. 3g). The elastic modulus was 18.6 kPa for SR and 29.9 kPa for SR/PDA based on the slopes in the range of strain 0–20%. The PDA crystals serve as a filler of the SR matrix. The increase in the elastic modulus originates from the interaction between the edge of the PDA crystal and the PDMS chain in a covalent manner. In this manner, SR/PDA was obtained by the homogenous dispersion of PDA in SR. On the other hand, the thermoresponsive color-changing properties of SR/PDA were the same as those of PDA (Fig. S3 in the SI). This indicates that the stimuli responsivity of PDA is not changed in the SR matrix.

Cascading responses in SR/PDA with DL

SR/PDA showed no color change response to the compression stress at 5 MPa (Fig. S4 in the SI). Cascading responses using DL are required to induce the color change of PDA. An aqueous solution containing PEI (linear polymer, $\bar{M}_w$ 3 × 10^2) was used as the interior liquid of DL.[40] The PEI concentration directing the color change of PDA was optimized prior to preparation of DL. A piece of SR/PDA of 10 × 10 × 3 mm in size was immersed for a certain period (t/h) in 10 cm^3 of the PEI aqueous solution in the range of 5–50 wt%. Photographs were taken at t = 0.5–29.5 h after starting the immersion (Fig. 4a and Fig. S5 in the SI). As faster color change was observed at higher concentrations, the PEI concentration was set at 50 wt% for preparing DL. In addition, DL was not formed using PEI solution concentration higher than 50 wt%. As the surface tension of the interior liquid is lowered with increasing PEI concentration to higher than 50 wt%, DL is not obtained due to wetting of the

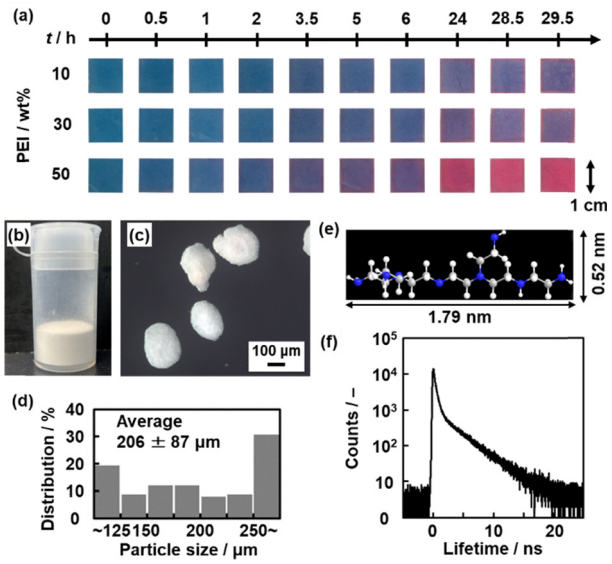

Fig. 4 Color-change properties of SR/PDA using DL containing PEI solution. (a) Photographs representing the relationship between the PEI concentration and immersion time for the color change of PDA in SR/PDA. (b) Photograph of DL stored in a polypropylene bottle. (c) Optical microscopy image of DL. (d) Size distribution of DL after sieving. (e) Schematic illustration of the PEI heptamer with a couple of branches. (f) PALS profile of SR/PDA.

solid powders with liquid. Therefore, the higher limit of the PEI concentration was set to 50 wt%. The intercalation of PEI in the interlayer space of the layered PDA induces the motion and torsion of the conjugated main chain, leading to the color change with shortening the effective conjugation length (Fig. 1e and f).[40]

DL was prepared by mixing 50 wt% PEI solution and PDMS-modified silica particles *ca.* 25 nm in size using the method provided in our previous reports (see the SI).[40,43] A free-flowing powder consisting of liquid droplets coated by silica particles was obtained and stored in a polypropylene bottle until use (Fig. 4b). White oval-shaped particles were observed on the optical microscopy image (Fig. 4c). The average diameter was 206 ± 87 μm after sieving to control the size (Fig. 4d). Cascading responses were demonstrated using DL and SR/PDA. About 50 mg of DL was homogenously sprinkled on SR/PDA of 10 × 10 × 3 mm in size (Fig. 5a). A compression stress of 0.1 kPa–5 MPa was applied for 120 s on the whole top face of DL/SR/PDA, contact area 10 × 10 mm, *via* a metallic probe using an automated tester. After releasing the stress, the uncollapsed DLs were removed using an air blower. The sample was maintained for 24 h at room temperature to promote the diffusion of PEI in the SR matrix. Then, the remaining DLs were washed off by ethanol. The SR/PDA device exhibited the color change to red (Fig. 5a).

The color change of PDA in SR indicates that PEI molecules are diffused into the inside of the SR matrix. In the present work, PEI with an average molecular weight $\bar{M}_w$ of 3×10^2 corresponds to the oligomers, such as heptamers and octamers, including a couple of branches. The size of the stretched chain is about 1.8 nm in length and 0.5 nm in diameter on the assumption of a heptamer with branches (Fig. 4e). The free volume space of SR was estimated using positron annihilation lifetime spectroscopy (PALS) (Fig. 4f and Table S1 in the SI). The radius of the free volume space is calculated to be r_3 = 0.39 nm by the third content of the annihilation lifetime on the assumption that the space is approximated by a sphere. As the diameter is estimated to be 0.78 nm, the space affords diffusion of the oligomeric PEI. In addition, the affinity of PEI to water and PDMS was calculated using the distance of Hansen similarity parameter (HSP). The HSP distance of PEI to PDMS (19.5) was smaller than that of PEI to water (27.3). The smaller HSP distance indicates the higher affinity. The micrometer-scale cracks and voids were not observed inside SR/PDA on the SEM image (Fig. S6 in the SI). These facts imply that the PEI oligomer can be penetrated into the SR matrix with diffusion in the free volume space. As the references, SR/PDA was immersed in the solution of PEI with the higher molecular weight ($\bar{M}_w$ values 6×10^2, 1.8×10^3, and 7.5×10^5) (Fig. S7 in the SI). The time to the color change was extended with increasing

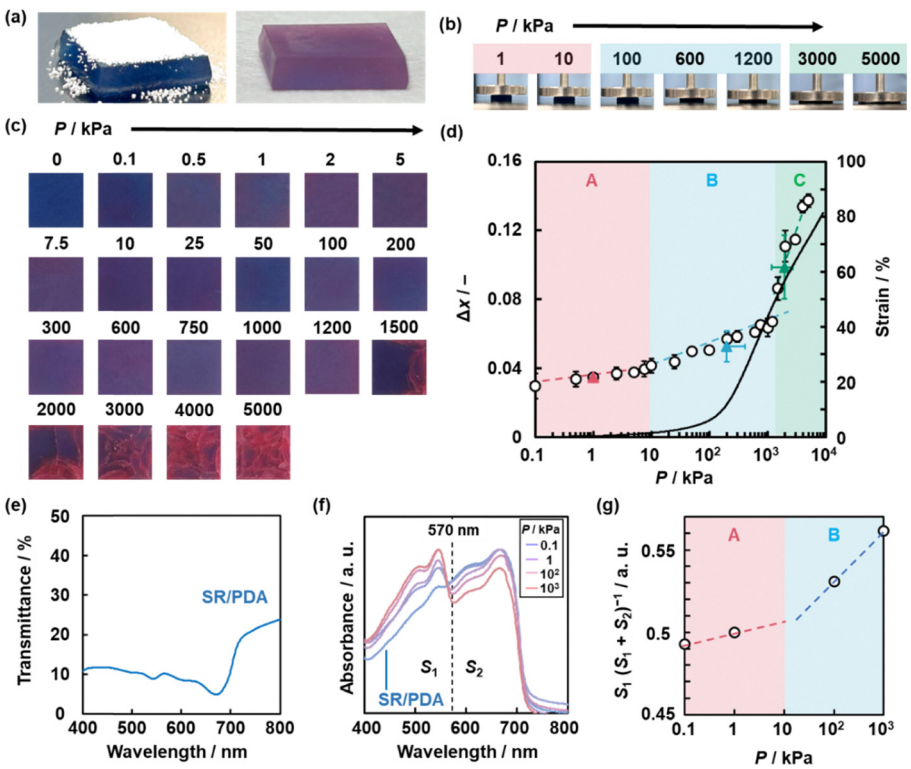

Fig. 5 Compression-responsive color-changing behavior of DL/SR/PDA. (a) Photographs of DL/SR/PDA before compressing (left) and SR/PDA with the color change (right). (b) Photographs of DL/SR/PDA during compressing at 1 kPa–5 MPa viewed from the side. (c) Top-view photographs of the device after compression at 0.1 kPa–5 MPa. (d) Relationship between P and Δx (left axis) with the stress–strain curve (right axis). (e) UV-vis transmission spectrum of SR/PDA 3 mm in thickness. (f) UV-vis absorption spectra of SR/PDA before compression and after compression 0.1, 1, 10^2, and 10^3 kPa. (g) Relationship between P and S_1 $(S_1 + S_2)^{-1}$.

the molecular weight. As the free volume space is dynamic with the molecular motion, PEI molecules can be migrated in the SR matrix and approached PDA. However, the diffusion rate of PEI with the longer chain and more branches is lowered in the free volume space because of the bulky molecular structure. In this manner, PEI is intercalated in the interlayer space of PDA dispersed in the SR matrix.

The XRD peaks characteristic of the layered structure disappeared after exposure to PEI solution (Fig. S8 in the SI). The size of PDA was not changed after the exposure to PEI (Fig. S8 in the SI). These results indicate that the periodic layered structure of PDA is deformed with the intercalation PEI in the interlayer space in a molecular scale. The similar results were observed in our previous work.[40] The color change of PDA is induced by the deformation of the layered structure.

Colorimetric sensing of compression stresses

Compression stress (P) in the range of 0.1 kPa–5 MPa was uniaxially applied to the whole top face of the DL/SR/PDA device for 120 s (Fig. 5b and c). The sample was maintained for 24 h. After removal of the remaining DLs, the photograph was taken on the top face of the device to calculate the red-color intensity (x) from RGB values using an international standard (Fig. 5c). The photographs exhibit that the red color intensity of the device increased with increasing P. An increment of x ($\Delta x = x - x_0$) was calculated based on the original value before the compression (x_0). The Δx values were calculated using three different DL/SR/PDA devices for each P to ensure the reproducibility (sample number $N = 3$, Fig. S9 and Table S2 in the SI). The relationship between P and Δx was summarized with the stress–strain curve of the device (Fig. 5d). The standard curves eqn (1)–(3) for the relationship between P and Δx were prepared in the regions A–C depending on the responsivity, respectively.

$$\Delta x = 0.0048 \log P + 0.0347 \quad (1)$$

$$\Delta x = 0.0122 \log P + 0.0282 \quad (2)$$

$$\Delta x = 0.105 \log P - 0.0247 \quad (3)$$

The quantitative relationship between P and Δx is applied to any device size and contact area. The x value based on the RGB one represents the ratio of the red-color intensity in the selected area. Therefore, the individual same values independent to the size of the area are read out for the initial x_0, observed x, and their differences (Δx). As the diffusion of PEI into SR was continued after 24 h, Δx increased with increasing the time to taking the photographs for the analysis of the color (Fig. S10 in the SI).

Mechanisms for colorimetric sensing

In the region A (P = 0.1–10 kPa), Δx increased with increasing the number of the disrupt DL. A reference DL was prepared using the same interior liquid containing an organic dye, 10^{-3} mol dm^{-3} rhodamine B, to estimate the number of the disrupt DL. When the colored DL was compressed on a white paper, the white area decreased in P = 0.1–10 kPa and then became nearly zero in P = 100 kPa–1 MPa (Fig. S11 and Table S3 in the SI). The decrease in the white area indicates that the number of the disrupt DL, *i.e.* the volume of the outflowed interior liquid, increased in P = 0.1–10 kPa. Based on the demonstration, the number of the disrupt DL corresponding to the color-changed area has a correlation with P in the region A (Fig. S12 in the SI). In the middle region B (P = 10 kPa–1 MPa), an increase in Δx is induced by the strain of the device (Fig. 5b). The strain correlates with P in this region B (Fig. S12 in the SI). In the regions A and B, the red-colored area in the depth direction was expanded with an increase in P (Fig. S13 in the SI). When SR/PDA is under the more strained state with stronger compression, the interior liquid is diffused into the deeper region. A steep increase in Δx was observed in the region C (P = 1–5 MPa). The photographs indicate the formation of cracks in SR/PDA (Fig. 5c). The length of the generated crack increased with increasing P (Fig. S13 in the SI). As the number of the generated cracks increases in the larger P, the diffusion of the interior liquid is promoted in SR. In the boundary between the regions B and C, both standard curves were applicable depending on the states whether the SR/PDA devices generated the cracks or not (Fig. S14 in the SI). The cracks were observed for four of nine devices at 1.5 MPa and six of nine devices at 2.0 MPa. When the cracks were not formed, the standard curve in the region B was applicable. The Δx values of the cracked devices show the trends in the standard curve in the region C. As the larger errors can be caused in the boundary between the regions B and C, the preferred ranges for the distribution imaging are in the regions A to B or C. In this manner, the applied P in the range of 0.1 kPa and 5 MPa can be colorimetrically quantified using three standard curves.

The color-change properties in the regions A and B were studied by UV-vis spectroscopy (Fig. 5e–g). The SR/PDA sample with 3 mm in thickness preserved the transparency in the visible-light region (Fig. 5e). The transparency indicates that the color change inside the SR matrix can be visible on the top-view image. The color-change behavior was analyzed by UV-vis diffuse-reflectance spectroscopy using an integrated sphere with white magnesium oxide as background (Fig. 5f).

The original blue-color SR/PDA had the broadened absorption with a peak at around 660 nm. Whereas the absorption around 660 nm decreased, that around 550 nm corresponding to red color increased with increasing P. When the peak areas of the absorption longer and shorter than 570 nm were defined as S_1 and S_2, respectively, the ratio of S_1 to the total area (S_1 $(S_1 + S_2)^{-1}$) increased with increasing P (Fig. 5g). The two-step increasing behavior of S_1 $(S_1 + S_2)^{-1}$ in the regions A and B is consistent with that of Δx in the standard curves (Fig. 5d and g). The UV-vis analyses corroborate that the number of the red-colored PDA increased in the SR matrix with increasing P.

The standard curves were applied to colorimetric estimation of unknown P (filled triangles in Fig. 5d and Fig. S15 and Table S4 in the SI). Simulated unknown P = 2.5 kPa, 250 kPa, and 2.5 MPa were applied under the same conditions to demonstrate the colorimetric sensing ($N = 3$ for each P). The measured P (P_{meas}) calculated using eqn (1)–(3) showed the

same order of the magnitude as the applied P. These results indicate that DL/SR/PDA device can be used for colorimetric sensing of compression stresses. Based on the standard curves, P_{meas} has deviations resulting from the standard deviation of the measured Δx for each device: ±2.00 kPa at 5 kPa, ±12.0 kPa at 50 kPa, ±63.0 kPa at 600 kPa, and ±425 kPa at 5 MPa. Although P_{meas} has deviations for each device, the red-colored area in the depth direction on the cross section (L_R) is almost constant in each device (Fig. S13 in the SI). The fact means the distribution of compression stress can be accurately imaged using the DL/SR/PDA device.

2D distribution imaging of compression stresses

When compression force is applied using 3D irregularly shaped objects to the 3D rubber device, the applied stress has distribution (Fig. 6 and Fig. S16 in the SI). Plastic ornaments of fruits, such as lemon, orange, and grape, were used to generate the millimeter-scale stress distribution (Fig. 6a). Compression forces (F/N) were applied to the DL/SR/PDA device 30 × 30 × 3 mm using these ornaments attached on the probe of an automated tester: F = 10 N for lemon, 40 N for orange, and 20 N for grape (Fig. 6b). The contacting areas were indicated by the dotted lines in the ornaments and devices (Fig. 6d–g). The photograph of the device was taken after the removal of the remaining DL. The image was divided into the frames 0.5 × 0.5 mm to calculate Δx in each frame. P was colorimetrically calculated from Δx in each frame and color-coded in the L_x–L_y coordinate (Fig. 6c–g). The standard curves (eqn (1)) and (eqn (2)) were used for the estimation of P (Fig. 6c). When F = 10 N was applied on the center of the DL/SR/PDA device using the lemon for 120 s, the applied stress had the distribution with the maximum near the center (Fig. 6d). On the other hand, when the top left was compressed at F = 10 N using the lemon under the same conditions (Fig. 6e), the distribution with the maximum was observed on the top left in the L_x–L_y coordinate. The orange with the more flattened contact area was used for compressing on the center at F = 40 N for 120 s (Fig. 6f). The distribution image exhibited the wider red-colored area compared with that of the lemon (Fig. 6d–f). When the probe was grape with the convex parts on the surface, the red-colored area was spread compared with that derived from the lemon and orange (Fig. 6g).

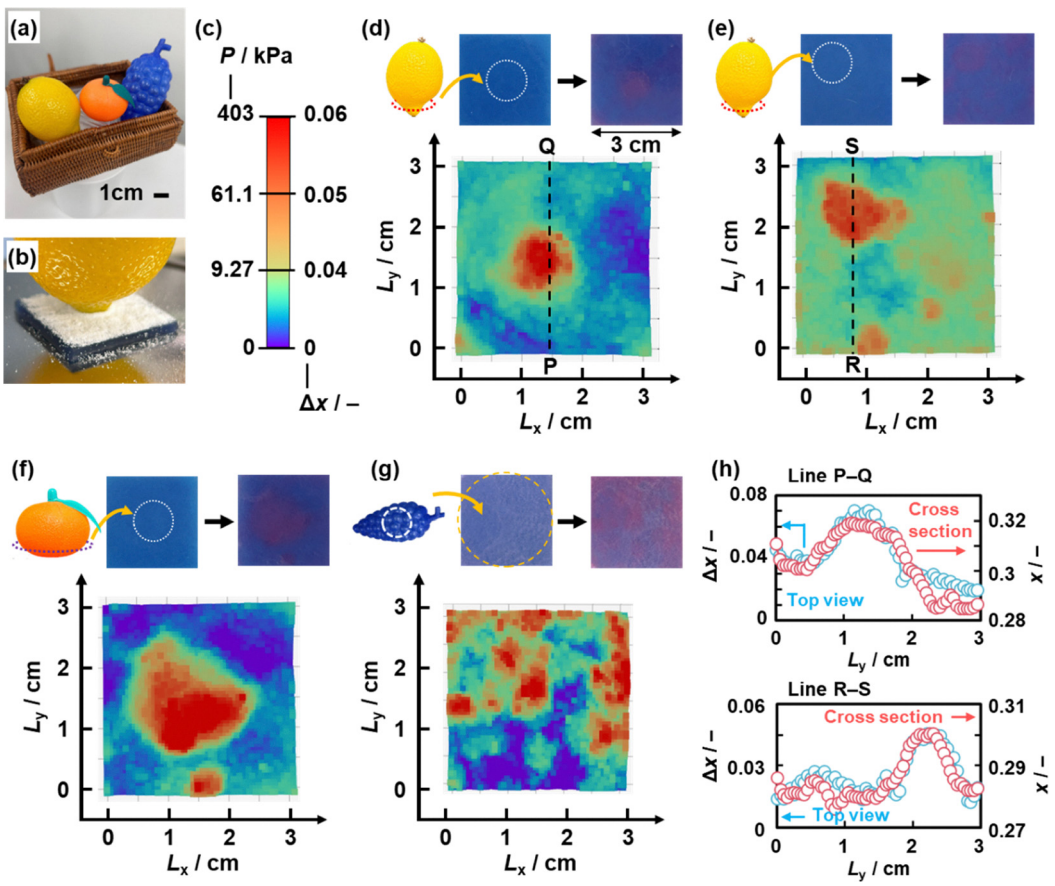

Fig. 6 2D distribution imaging of compression stresses applied by 3D objects. (a) Plastic ornaments of lemon, orange, and grape. (b) Photograph of DL/SR/PDA with compression using the lemon. (c) Color-coded profile representing the relationship between P and Δx based on the standard curves. (d) and (e) Photographs before and after compression (upper) and mapping image (lower) with contacting and compressing at the dotted-line area using the lemon at 10 N s on the center (d) and left below (e). (f) and (g) Photographs before and after compression (upper) and mapping image (lower) with contacting and compressing at the dotted-line area using the orange at 40 N (f) and grape (g) at 20 N at the center. (h) Line profiles of Δx on the top view (blue, left axis) and x on the cross-sectional view (red, right axis) in the lines P–Q (panel (d)) and R–S (panel (e)).

The line profiles of the stress distribution were prepared using the two different methods to validate the imaging (Fig. 6h). The profile was prepared in the lines P–Q and R–S using the top-view images (blue plots in Fig. 6h). The frames 0.5 × 0.5 mm were prepared to calculate Δx in the lines P–Q and R–S in Fig. 6d and Fig. 6e, respectively. As a reference, the device was cut in these lines to expose the cross-section (Fig. S17 in the SI). The x value was calculated on the cross-section dividing the area into 0.5 mm in width and 3 mm in height (red plots in Fig. 6h). The variation of Δx in the top view and x in the cross-sectional image are consistent with each other (Fig. 6h). The fact supports the validity of the stress-distribution imaging.

The 3D transparent device with sufficient thickness and softness enables 2D distribution imaging of compression stresses applied by 3D irregular shapes. Although a limited number of previous works showed stress-distribution imaging (Fig. S1 in the SI),[19–22] such 3D irregular shaped objects were not used as the probe for compression. The present work indicates that 3D device with sufficient thickness, transparency, and softness are required to achieve such distribution imaging. Moreover, DL/SR/PDA had the wider detection range to the compression stresses (0.1 kPa–5 MPa) compared with that of the other materials and devices in the previous reports (Fig. S1 in the SI). Our device has three different responsive mechanisms providing three standard curves. Therefore, wider responsivity is achieved in a single device.

Conclusions

A 3D transparent soft DL/SR/PDA device was prepared for 2D distribution imaging of compression stresses applied by 3D irregularly shaped objects. DL as a compression-responsive capsule was set on the transparent SR bulk matrix containing the layered PDA. Disorganization of DL with compression induced the outflow of the interior liquid containing PEI. The outflowed PEI oligomer is diffused into the SR matrix in the free volume space and then intercalated into the interlayer space of the layered PDA. The cascading responses induced the color change to red. The red-color intensity increased with increasing P in the range of 0.1 kPa–5 MPa. As the relationship between P and Δx was represented by the three different standard curves, unknown P was colorimetrically estimated from Δx. The 3D DL/SR/PDA device enabled 2D distribution imaging of compression stresses applied by the ornaments of fruits in the millimeter to the centimeter scales. The present work shows that 2D stress imaging can be achieved using a sensing device with transparency and flexible 3D shape. A cascading response combining multiple stimuli-responsive materials is applied to expand the range and type of the applied stress. These concepts of the device design can be applied in the development of various stress-imaging devices in different ranges and scales.

Conflicts of interest

There are no conflicts to declare.

Data availability

The data supporting this article have been included as part of the supplementary information (SI). Supplementary information: experimental methods, summary of the related previous works, color-change properties of the reference samples, SEM images, and PALS analysis. See DOI: https://doi.org/10.1039/d5mh02253c.

Acknowledgements

This work was partially supported by JSPS-KAKENHI (Y. O. JP22H02148), Asahi Glass Foundation, and Japan Agency for Medical Research and Development (AMED, JP23ym01268 113j0002 and JP25ym0126819).

Notes and references

1 D. T. Butcher, A. Alliston and V. M. A. Weaver, *Nat. Rev. Cancer*, 2009, **9**, 108.
2 Y. Zang, F. Zhang, C. Di and D. Zhu, *Mater. Horiz.*, 2015, **2**, 140.
3 C. Xu, J. Chem, Z. Zhu, M. Liu, R. Lan, X. Chen, W. Tang, Y. Zhang and H. Li, *Small*, 2024, **20**, 2306655.
4 B. V. Asya, S. Wang, E. Euchelr, V. N. Khiêem and R. Göstl, *Aggregate*, 2025, **6**, e70014.
5 K. V. Meena and A. R. Sankar, *IEEE Sens. J.*, 2021, **21**, 10241.
6 G. A. Holzapfel, J. D. Humphrey and R. W. Ogden, *J. R. Soc., Interface*, 2025, **22**, 20240361.
7 Z. Chen, F. Zhang, X. Qian, G. Zhao and Z. Yang, *Mater. Horiz.*, 2025, **12**, 7894.
8 H. Qiao, S. Sun and P. Wu, *Adv. Mater.*, 2023, **35**, 2300593.
9 J. Su, K. He, Y. Li, J. Tu and X. Chen, *Chem. Rev.*, 2025, **125**, 5848.
10 N. Kopiika and Y. Blikharskyy, *Struct. Control. Health Monit.*, 2024, 1763285.
11 M.-h Park, S. Yako, Y. Takeda, A. Shibata and N. Tsuji, *Scr. Mater.*, 2024, **252**, 116264.
12 M. M. Caruso, D. A. Davis, Q. Shen, S. A. Odom, N. R. Sottos, S. R. White and J. S. Moore, *Chem. Rev.*, 2009, **109**, 5755.
13 Y. Sagara and T. Kato, *Nat. Chem.*, 2009, **1**, 605.
14 J. M. Clough, C. Weder and S. Schrettl, *Macromol. Rapid Comm.*, 2021, **42**, 2000528.
15 T. Seki, M. Hoshino, Y. Suzuki and S. Hayashi, *CrystEngComm*, 2021, **23**, 5686.
16 K. Ariga, *Small Methods*, 2022, **6**, 2101577.
17 K. Tanaka and Y. Chujo, *Polym. J.*, 2023, **55**, 353.
18 T. Watabe and H. Ohtsuka, *Macromolecules*, 2024, **57**, 425.
19 R. Hong, Y. Shi, X. Q. Qang, L. Peng, X. Wu, H. Cheng and S. Chen, *RSC Adv.*, 2017, **7**, 33258.
20 H. Yi, S.-H. Lee, H. Ko, D. Lee, W. G. Bae, T. I. Kim, D. S. Hwang and H. E. Jeong, *Adv. Funct. Mater.*, 2019, **22**, 1902720.
21 C. H. Wu, C. W. Tu, J. Aimi, J. Zhang, T. Chen, C. C. Wang and C. F. Huang, *Polym. Chem.*, 2020, **11**, 6423.
22 T. Yamakado and S. Saito, *J. Am. Chem. Soc.*, 2022, **144**, 2804.

23 Z. Xu, M. Liu, Y. Liu, Y. Pan, L. Yang and D. Ge, *ACS Appl. Mater. Interfaces*, 2023, **15**, 3673.
24 N. Ono, R. Seishima, K. Okabayashi, H. Imai, S. Fujii and Y. Oaki, *Adv. Sci.*, 2023, **10**, 2206097.
25 Y. Takeuchi, H. Imai and Y. Oaki, *J. Mater. Chem. C*, 2025, **13**, 3209.
26 Y. Mochizuki, H. Imai and Y. Oaki, *ACS Appl. Mater. Interfaces*, 2023, **15**, 48725.
27 N. Ono, R. Seishima, K. Shigeta, K. Okabayashi, H. Imai, S. Fujii and Y. Oaki, *Small*, 2024, **20**, 2400938.
28 R. W. Carpick, D. Y. Sasaki, M. S. Marcus, M. A. Eriksson and A. R. Burns, *J. Phys.: Condens. Matter*, 2004, **16**, R679.
29 B. Yoon, S. Lee and J. M. Kim, *Chem. Soc. Rev.*, 2009, **38**, 1958.
30 X. Sun, T. Chen, S. Huang, L. Li and H. Peng, *Chem. Soc. Rev.*, 2010, **39**, 4244.
31 R. Jelinek and M. Ritenberg, *RSC Adv.*, 2013, **3**, 21192.
32 X. Qian and B. Städler, *Chem. Mater.*, 2019, **31**, 1196.
33 Y. Oaki, *Chem. Commun.*, 2020, **56**, 13069.
34 B. Das, S. Jo, J. Zheng, J. Chen and K. Sugihara, *Nanoscale*, 2022, **14**, 1670.
35 Z. Yu, C. MuYu, H. Xu, J. Zhao and G. Yang, *Polym. Chem.*, 2023, **14**, 2266.
36 Y. Kim, K. Iimura and N. Tamaoki, *Bull. Chem. Soc. Jpn.*, 2024, **97**, uoae034.
37 L. Juhasz, R. D. Ortuso and K. Sugihara, *Nano Lett.*, 2021, **21**, 543.
38 H. Terada, H. Imai and Y. Oaki, *Adv. Mater.*, 2018, **30**, 1801121.
39 Y. Oaki and S. Fujii, *Chem. Commun.*, 2024, **60**, 9163.
40 M. Nakamitsu, K. Oyama, H. Imai, S. Fujii and Y. Oaki, *Adv. Mater.*, 2021, **33**, 2008755.
41 D. H. Park, J. Hong, I. S. Park, C. W. Lee and J. M. Kim, *Adv. Funct. Mater.*, 2014, **24**, 5186.
42 L. Jayes, A. P. Hard, C. Séné, S. F. Parker and U. A. Jayasooriya, *Anal. Chem.*, 2003, **75**, 742.
43 K. Kido, T. Sumoto, Y. Yasui, Y. Nakamura and S. Fujii, *Adv. Powder Technol.*, 2017, **28**, 1977.

